DAAM2 Variants Cause Nephrotic Syndrome via Actin Dysregulation

Ronen Schneider,[1,15] Konstantin Deutsch,[1,15] Gregory J. Hoeprich,[2] Jonathan Marquez,[3] Tobias Hermle,[4] Daniela A. Braun,[1] Steve Seltzsam,[1] Thomas M. Kitzler,[1] Youying Mao,[1] Florian Buerger,[1] Amar J. Majmundar,[1] Ana C. Onuchic-Whitford,[1,5] Caroline M. Kolvenbach,[1] Luca Schierbaum,[1] Sophia Schneider,[1] Abdul A. Halawi,[1] Makiko Nakayama,[1] Nina Mann,[1] Dervla M. Connaughton,[1] Verena Klämbt,[1] Matias Wagner,[6,7] Korbinian M. Riedhammer,[6,8] Lutz Renders,[8] Yoshichika Katsura,[9] Dean Thumkeo,[9] Neveen A. Soliman,[10,11] Shrikant Mane,[12] Richard P. Lifton,[13,14] Shirlee Shril,[1] Mustafa K. Khokha,[3] Julia Hoefele,[6] Bruce L. Goode,[2] and Friedhelm Hildebrandt[1,*]

Summary

The discovery of >60 monogenic causes of nephrotic syndrome (NS) has revealed a central role for the actin regulators RhoA/Rac1/ Cdc42 and their effectors, including the formin INF2. By whole-exome sequencing (WES), we here discovered bi-allelic variants in the formin DAAM2 in four unrelated families with steroid-resistant NS. We show that DAAM2 localizes to the cytoplasm in podocytes and in kidney sections. Further, the variants impair DAAM2-dependent actin remodeling processes: wild-type DAAM2 cDNA, but not cDNA representing missense variants found in individuals with NS, rescued reduced podocyte migration rate (PMR) and restored reduced filopodia formation in shRNA-induced DAAM2-knockdown podocytes. Filopodia restoration was also induced by the formin-activating molecule IMM-01. DAAM2 also co-localizes and co-immunoprecipitates with INF2, which is intriguing since variants in both formins cause NS. Using in vitro bulk and TIRF microscopy assays, we find that DAAM2 variants alter actin assembly activities of the formin. In a Xenopus daam2-CRISPR knockout model, we demonstrate actin dysregulation in vivo and glomerular maldevelopment that is rescued by WT-DAAM2 mRNA. We conclude that DAAM2 variants are a likely cause of monogenic human SRNS due to actin dysregulation in podocytes. Further, we provide evidence that DAAM2-associated SRNS may be amenable to treatment using actin regulating compounds.

Introduction

Steroid-resistant nephrotic syndrome (SRNS) is characterized by edema, nephrotic-range proteinuria (urine protein excretion > 50 mg/kg per day), hypoalbuminemia, and hyperlipidemia. It represents the second most frequent cause of chronic kidney disease before the age of 30.[1] Variants in more than 60 different genes have been discovered as monogenic causes of SRNS.[2–7] Interestingly, most variants implicated in SRNS are found in highly expressed genes in the glomerular podocytes,[8–10] implicating podocytes as the primary site of injury in NS and highlighting their role in maintaining the filtration barrier. The actin network in podocytes is essential for maintaining intact foot process architecture in several ways: for formation of the unique arborization of podocyte foot processes,[11,12] for maintaining the slit diaphragm turnover through pro-moting endocytosis[13] and the formation of stress fibers,[14] and by providing physical support of the complex podocyte morphology under variable glomerular pressures.[12,15] In addition, recent findings indicate that actin interacting proteins are prevalent among the monogenic causes of SRNS, pointing to actin playing a central role in podocyte physiology.[16–19]

Many key aspects of actin cytoskeleton dynamics are regulated by upstream small GTPases: RhoA, Rac1, and Cdc42.[20–24] Variants in genes encoding actin regulators or effectors of the Rho/Rac/Cdc42 pathway have been associated with monogenic nephrotic syndrome in human individuals and with NS mouse models.[16,17,25–30] Formins are Rho/Rac/Cdc42 effectors that regulate actin polymerization.[31–34] In mammals, there are 15 different formin genes/proteins, which fall into seven subfamilies: Dia, Daam, FMNL, FHOD, INF, FMN, and Delphilin.[35,36] The

[1]Department of Pediatrics, Boston Children's Hospital, Harvard Medical School, Boston, MA 02115, USA; [2]Department of Biology, Brandeis University, Waltham, MA 02454, USA; [3]Pediatric Genomics Discovery Program, Department of Pediatrics and Genetics, Yale University School of Medicine, New Haven, CT 06520, USA; [4]Renal Division, Department of Medicine, Faculty of Medicine and Medical Center, University of Freiburg, Freiburg 79106, Germany; [5]Renal Division, Brigham and Women's Hospital, Harvard Medical School, Boston, MA 02115, USA; [6]Institute of Human Genetics, Klinikum rechts der Isar, School of Medicine, Technical University of Munich, Munich 81675, Germany; [7]Institute of Neurogenomics, Helmholtz Zentrum München, Neuherberg 85764, Germany; [8]Department of Nephrology, Klinikum rechts der Isar, School of Medicine, Technical University of Munich, Munich 81675, Germany; [9]Department of Drug Discovery Medicine, Medical Innovation Center, Kyoto University Graduate School of Medicine, Kyoto 606-8507, Japan; [10]Department of Pediatrics, Center of Pediatric Nephrology & Transplantation, Kasr Al Ainy School of Medicine, Cairo University, Cairo 11562, Egypt; [11]Egyptian Group for Orphan Renal Diseases (EGORD), Cairo, Egypt; [12]Department of Genetics, Yale University School of Medicine, New Haven, CT 06520, USA; [13]Laboratory of Human Genetics and Genomics, the Rockefeller University, New York, NY 10065-6399, USA; [14]Howard Hughes Medical Institute, Chevy Chase, MD 20815-6789, USA
[15]These authors contributed equally
*Correspondence: friedhelm.hildebrandt@childrens.harvard.edu
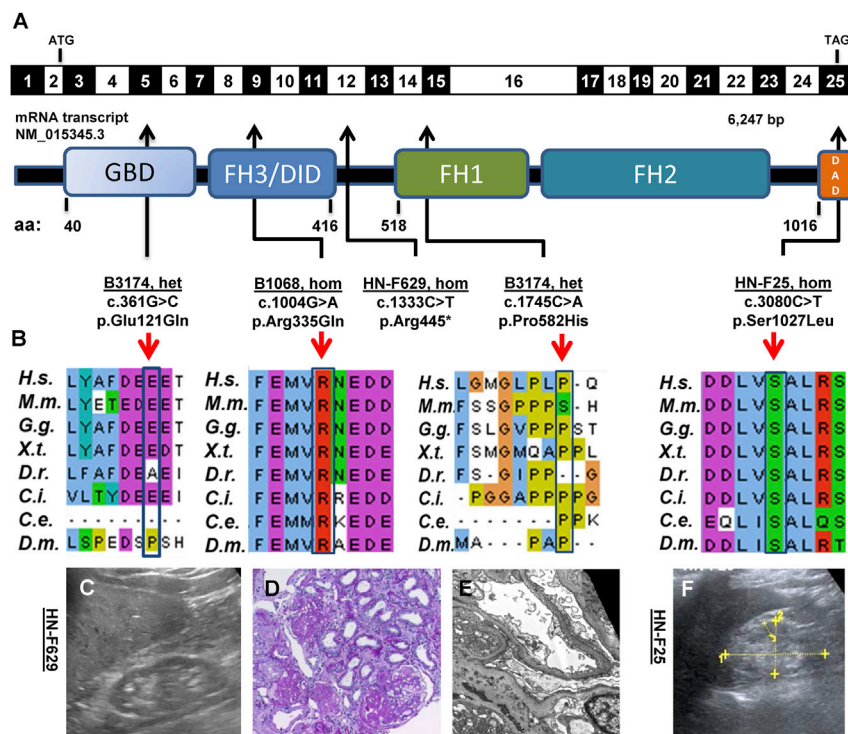https://doi.org/10.1016/j.ajhg.2020.11.008.

Figure 1. Whole-Exome Sequencing Identifies Recessive Disease-Causing Variants in *DAAM2* in Four Families with SRNS

(A) Schematic of DAAM2 cDNA and the corresponding protein, including its functional domains. Arrows indicate the position of five variants of *DAAM2* that were identified by whole-exome sequencing (WES) in four families (B3174, B1068, HN-F629, and HN-F25) with nephrotic syndrome.

(B) Alignment of amino acid sequence of DAAM2 conservation down evolution for each altered amino acid residue for each of the missense variants found.

(C–E) Renal ultrasound image (C), renal histology (Trichrome staining) (D), and electron microscopy (E) of individual HN-F629, show hyperechogenic right kidney, FSGS, and foot process effacement.

(F) Renal US image of individual HN-F25 showing hyperechogenic right kidney.

aa, amino acid; DAD, diaphanous autoregulatory domain; DID, diaphanous inhibitory domain; FH1, Formin homology domain 1; FH2, Formin homology domain 2 GDB, GTPase binding domain; H.s., *Homo sapiens*; M.m., *Mus musculus*; G.g. *Gallus gallus*; X.t., *Xenopus tropicalis*; D.r., *Danio rerio*; C.i., *Ciona intestinalis*; C.e., *Caenorhabditis elegans*; D.m. *Drosophila melanogaster*.

N-terminal halves of formins can be diverse and mediate specific molecular interactions that direct formins to different subcellular locations and control formin activities[37,38] (Figure 1A). The C-terminal halves of formins are more highly conserved and consist of the formin homology 1 and 2 (FH1 and FH2) domains, followed by "tail" regions (Figure 1A). These FH1-FH2-tail portions of formins directly nucleate actin filament assembly and remain processively attached to the growing barbed end of the filament while accelerating elongation in a profilin-dependent manner.[33] Formin effects on actin assembly are tightly regulated *in vivo*. Five out of the seven formin subfamilies (including Dia and Daam) are regulated by auto-inhibition, through interactions of their N-terminal diaphanous inhibitory domains (DID) with C-terminal diaphanous autoregulatory domains (DAD).[39–41] DID-DAD interactions maintain these formins in an inactive state until ligands (e.g., RhoA) trigger the release of formins from auto-inhibition, leading to actin assembly.[39,40,42–44]

Actin assembly by diaphanous related formins (Dia formins or DRFs) is also modulated by Inverted Formin 2 (INF2),[45] variants of which are well-studied autosomal-dominant causes of SRNS (MIM: 610982).[30] In addition, actin assembly itself triggers downstream changes in gene expression through the transcription factor serum response factor (SRF), resulting in upregulation of cytoskeletal regulatory proteins.[45] Many of these proteins are highly expressed in podocytes and have been implicated in human NS cases (*INF2*, *MYH9* [MIM: 155100], *ACTN4* [MIM: 604638])[27,28,30] and murine NS models (*Tln1*, *Cfl1*, *Tjp1*,

Srf, and *Mkl1/2*),[46–49] further highlighting the importance of tight actin regulation for podocyte function.

Because a monogenic cause of SRNS can be found by whole-exome sequencing (WES) in 11%–45% of families, by detecting a variant in one of the >60 published genes,[2–6] we hypothesized that novel single-gene etiologies may exist in subjects without a molecular diagnosis. Therefore, to identify novel monogenic causes of SRNS and to further understand its pathogenesis, we applied WES to individuals with SRNS and identified variants in *DAAM2* in four unrelated families, and we characterized the related pathogenesis in SRNS.

Material and Methods

Study Approval

Approval for human subject research was obtained from the University of Michigan and the Boston Children's Hospital Institutional Review Boards and the Technical University of Munich review board. All participants or their guardians provided written informed consent.

Study Participants

Following informed consent, clinical data and blood samples were obtained from individuals with SRNS. The diagnosis of NS was made by (pediatric) nephrologists, based on standardized clinical and renal histologic criteria. Renal biopsies were evaluated by renal pathologists. Clinical data were obtained using an established questionnaire.

Homozygosity Mapping, Whole-Exome Sequencing, and Variant Calling

Homozygosity mapping, whole-exome sequencing, and variant calling were performed as described previously.[50,51]

Plasmids, siRNAs, shRNA, Cell Culture, and Transfection

Human full-length *DAAM2* cDNA was subcloned following PCR from human full-length cDNA (GeneScript, OHu13890). Mouse *Daam2* was subcloned following PCR from murine full-length cDNA (GeneScript, OMu20712). For mutant p.Pro582His, we created an shRNA-resistant human cDNA clone by site directed mutagenesis, since mouse has no proline in the corresponding position. Truncation constructs and mutant constructs were generated by PCR. Primers are shown Table S1. The following expression vectors were used: pRK5-N-Myc, pCDNA6.2-N-GFP, and pSirenRetroQ. Clones reflecting the variants identified in individuals with SRNS were introduced into the cDNA constructs using Quik change II XL site-directed mutagenesis kit (Agilent Technologies). The *DAAM2*-specific and control scrambled siRNAs were purchased from GE Dharmacon. Overexpression experiments were performed in HEK293T cells (ATCC biological resource center) and in immortalized human podocytes that were a gift from Dr. Moin Saleem (University of Bristol, Bristol, UK).

HEK cells were maintained in DMEM, supplemented with 10% fetal bovine serum, 50 IU/mL penicillin, and 50 μg/mL streptomycin. Podocytes were maintained in RPMI plus GlutaMAX-I (GIBCO) supplemented with 10% fetal bovine serum, 50 IU/mL penicillin/50 μg/mL streptomycin, and insulin-transferrin-selenium-X.

Plasmids and siRNAs were transfected into HEK293T cells or podocytes at 37°C using Lipofectamine 2000 (Invitrogen). Podocytes were grown at the permissive temperature of 33°C. RNAi knockdown in human podocyte cell lines employed pSirenRetroQ with 2 independent shRNA directed against human *DAAM2* using retroviral transduction. Puromycin was used to select transduced cells. Knockdown efficiency was confirmed for all experiments. (shRNA targets are shown Table S1, knockdown efficiency was confirmed, see Figure S3D). For rescue experiments, knockdown podocytes underwent a transient transfection using murine *DAAM2* constructs. All cell lines were tested weekly and found negative for the presence of mycoplasma.

Immunoblotting, Immunoprecipitation, Pull-Down Assay, and Immunofluorescence Staining

Immunoblotting, immunoprecipitation, and immunofluorescence staining were performed as described previously.[52] Briefly, HEK293T were lysed and pre-cleared using rec-Protein A-Sepharose 4B Conjugate (Life Technologies) overnight. Then, equal amounts of protein were incubated with EZview Red Anti-c-Myc Affinity Gel (Sigma-Aldrich) or GFP-nAb (Allele Biotechnology). Coimmunoprecipitation experiments were performed in two independent experiments. Immunoblotting was performed using rabbit anti-*DAAM2* (ab169527, abcam; PA5-23201, Invitrogen; A7463, Abclonal; and HPA051300, Sigma-Aldrich) and custom made rabbit anti-DAAM2 (Boston Molecules) and with mouse anti-DAAM2 (sc-515129, Santa Cruz Biotechnology), mouse anti-c-Myc (sc-40, Santa Cruz Biotechnology), rabbit anti-c-Myc (sc-789, Santa Cruz Biotechnology), mouse anti-GFP (sc-9996, Santa Cruz Biotechnology), rabbit anti-GFP (sc-8334, Santa Cruz Biotechnology). Immunofluorescence of DAAM2 was performed with rabbit anti-DAAM2 (ab169527, abcam; Custom, Boston Mol-

ecules). Fluorescent images were obtained with a Leica SP5X laser scanning microscope.

Filopodia Assay

Cultured human podocytes were plated on a 6-well plate (70k cells/condition). Cells were transfected with GFP-tagged cDNA clones of DAAM2 (wild type or harboring human variants) and then imaged hourly by the IncuCyte Videomicroscopy system over 24 h, using green channel. Number of "filopodia-forming" cells (cells forming two or more cellular extensions) were counted at time points 10, 15, and 20 h post transfection, and a ratio of positive cells to total transfected cells (green signal detected), were calculated. For drug experiments, 10 mg of IMM01 was dissolved in 1 mL of DMSO for a final concentration of 37.4 mM. Next, calculated volumes of drug stock were added to podocyte growth medium resulting in final concentrations of 1–200 μM.

Podocyte Migration Assay

Real-time migration assay was performed using the IncuCyte Videomicroscopy system (Essen Bioscience) in 96-well plates according to the manufacturer's instructions. Briefly, 24 h after transfection (2 μg/cDNA plasmid) scratch-wounds were made using a 96-pin tool (Woundmaker) as per protocol. Cells were monitored automatically via live cell imaging and time-lapse images. Wound confluency was automatically acquired hourly and recorded by the IncuCyte software (ZOOM). Data processing and analysis for migration assay were performed using the IncuCyte 96-well Kinetic Cell Migration and Invasion Assay software module. Results are presented as time versus wound confluency.

Purification and Labeling of Actin

Rabbit skeletal muscle actin was purified from acetone powder[53] generated from frozen ground hind leg muscle tissue of young rabbits (PelFreez). Lyophilized acetone powder stored at −80°C was mechanically sheared in a coffee grinder, resuspended in G-buffer (5 mM Tris-HCl [pH 7.5], 0.5 mM Dithiothreitol [DTT], 0.2 mM ATP, 0.1 mM $CaCl_2$), and then cleared by centrifugation for 20 min at $50,000 \times g$. The supernatant was filtered through Grade 1 Whatman paper, then the actin was polymerized by the addition of 2 mM $MgCl_2$ and 50 mM NaCl and incubated overnight at 4°C. The final NaCl concentration was adjusted to 0.6 M to strip residual actin-binding proteins, incubated at 4°C for 1 h, and then the F-actin was pelleted by centrifugation for 150 min at $361,000 \times g$. The pellet was solubilized by dounce homogenization and dialyzed against 1 L of G-buffer at 4°C (three consecutive times at 12–18 h intervals). Monomeric actin was then precleared at $435,000 \times g$ and loaded onto a S200 (16/60) gel-filtration column (GE Healthcare) equilibrated in G-Buffer. Peak fractions containing actin were stored at 4°C.

To fluorescently label actin, G-actin was polymerized by dialyzing overnight against modified F-buffer (20 mM PIPES [pH 6.9], 0.2 mM $CaCl_2$, 0.2 mM ATP, 100 mM KCl).[54] F-actin was incubated for 2 h at room temperature with Alexa 488 NHS ester dye (Life Technologies) at a final molar concentration 5 times in excess of actin concentration. F-actin was then pelleted by centrifugation at $450,000 \times g$ for 40 min at room temperature. The pellet was resuspended in G-buffer, homogenized with a dounce, incubated on ice for 2 h to depolymerize filaments. Actin was then re-polymerized on ice for 1 h after adding KCl and $MgCl_2$ (final concentration of 100 mM and 1 mM, respectively). F-actin was pelleted by centrifugation for 40 min at $450,000 \times g$ at 4°C. The pellet was

homogenized with a dounce and dialyzed overnight at 4°C against 1 L of G-buffer. Next, the solution was centrifuged at 450,000 × g for 40 min at 4°C. The supernatant was collected and the concentration and labeling efficiency was determined by measuring the absorbance at 280 nm and 495 nm. Molar extinction coefficients used were as follows: ε_{280} actin = 45,840 M^{-1} cm^{-1}, ε_{495} Alexa 488 = 71,000 M^{-1} cm^{-1} and ε_{280} Alexa488 = 7,810 M^{-1} cm^{-1}.

Purification of Daam2 Polypeptides

GST-SNAP-C-Daam2 polypeptides (FH1-FH2-tail domains) (WT or p.Ser1027Leu) and GST-N-Daam2 (WT or p.Arg335Gln [c.1004G>A]) polypeptides were expressed in *E. coli* strain BL21 pRARE (Novagen). Cells were grown at 37°C in TB medium to log phase (OD$_{600}$ = 1.5), then expression was induced by the addition of 0.4 mM IPTG, and cells were grown overnight at 18°C. Cells were harvested by centrifugation and pellets were stored at −80°C. Frozen pellets were resuspended in lysis buffer (50 mM potassium phosphate [pH 8.0], 300 mM KCl, 1 mM DTT, 50 mM imidazole, 1% Triton, and 1 mM PMSF) supplemented with a protease inhibitor cocktail (0.5 μM each of pepstatin A, antipain, leupeptin, aprotinin, and chymostatin). Cells were lysed with lysozyme (1 mg/mL, 0.5 mM EDTA) for 30 min at 4°C rotating. The lysate was cleared by centrifugation at 150,000 × g for 30 min at 4°C. The supernatant was then loaded on a GSTrap-FF 1 mL column (GE Healthcare) using a Fast Protein Liquid Chromatography (FPLC) system. The column was washed with 5 column volumes of washing buffer (20 mM Tris [pH 8.0], 150 mM KCl, 5% glycerol), and then PreScission protease (GE Healthcare) was introduced onto the column and allowed to incubate overnight at 4°C to cleave the GST-tag. The liberated Daam2 polypeptides were then eluted from the column, concentrated, and loaded on a Superose 12 10/300 GL (GE Healthcare) in HEKG$_5$ buffer (20 mM HEPES [pH 8.0], 1 mM EDTA, 50 mM KCl, 5% glycerol). Peak fractions were concentrated, aliquoted, snap frozen in liquid N$_2$, and stored at -80°C.

Purification of Spectrin-Actin Seeds

Spectrin-actin complexes were purified essentially as described.[55] Briefly, 20 mL of packed human red blood cells (Novaseek Research) were washed with three times with 25 mL of ice-cold Buffer A (5 mM sodium phosphate [pH 7.7], 150 mM NaCl, and 1 mM EDTA), each time centrifuging for 15 min at 2,000 × g at 4°C, and discarding the supernatant. To lyse cells, the cell pellet was resuspended in 700 mL (approximately 10 times the volume of washed cells) of ice-cold lysis buffer (5 mM sodium phosphate [pH 7.7] and 1 mM PMSF) and incubated for 40 min while stirring at 4°C. The lysate was centrifuged for 15 min at 45,000 × g at 4°C. The cloudy and viscous pellets were resuspended in wash buffer B (5 mM sodium phosphate [pH 7.7] and 0.1 mM PMSF), final volume 360 mL, and homogenized by pipetting. Next, the mixture was centrifuged for 15 min at 45,000 × g at 4°C. The pellets were resuspended in a total volume of 180 mL of wash buffer B and homogenized as above, then centrifuged as above. This process was repeated once more. Pellets are translucent at this stage. Next, the Spectrin-actin was extracted by resuspending each pellet in 5 mL of extraction buffer (0.3 mM sodium phosphate [pH 7.6] and 0.1 mM PMSF), combining the contents into one tube, adjusting the volume to 60 mL with the same buffer, and centrifuging for 30 min at 60,000 × g at 4°C, repeated once. The final pellet was resuspended in an equal volume of extraction buffer and gently vortexed, then incubated for 40 min in a water bath at 37°C while manually inverting the tubes every ~10 min. Finally,

the sample was precleared for 30 min at 450,000 × g at 4°C. DTT (2 mM final) and protease inhibitors were added to the cleared supernatant, and an equal volume of cold glycerol (50% final concentration) was mixed into the solution. Spectrin-actin seeds were aliquoted and stored at –20°C.

Purification of Profilin

Human Profilin-1 was expressed in *E. coli* BL21 DE3 by growing cells to log phase (OD$_{600}$ = 1.5) at 37°C in TB medium, then inducing expression using 0.4 mM IPTG at 37°C for 3 h. Cells were harvested by centrifugation and pellets were stored at −80°C. Cell pellets were resuspended in lysis buffer (50 mM Tris-HCl [pH 8.0], 1 mM EDTA, 0.2% Triton X-100, lysozyme, and protease inhibitors as described above), kept at 4°C rotating for 30 min. Lysates were cleared for 30 min at 272,000 × g at 4°C, and the supernatant was collected and loaded on a HiTrap Q column equilibrated in 20 mM Tris-HCl (pH 8.0), followed by a Superdex 75 column equilibrated in 20 mM Tris-HCl (pH 8.0) and 50 mM NaCl. Peak fractions were pooled, snap frozen in aliquots, and stored at −80°C.

Microfluidics-Assisted TIRF Microscopy

Actin filament polymerization was monitored by microfluidics-assisted Total Internal Reflection Microscopy (mf-TIRF).[54,56,57] Coverslips were first cleaned by sonication in detergent for 60 min, followed by successive sonications in 1 M KOH and 1 M HCl for 20 min each and in ethanol for 60 min. Coverslips were then washed extensively with H$_2$O and dried in an N$_2$ stream. The cleaned coverslips were coated with a 80% ethanol solution adjusted to pH 2.0 with HCl containing 2 mg/mL mPEG-silane, MW 2,000, and 2 μg/mL Biotin-PEG-silane, MW 3,400 (Laysan Bio) and incubated overnight at 70°C. A 40 μm high PDMS mold with 3 inlets and 1 outlet was mechanically clamped onto a PEG-Silane-coated coverslip. The chamber was then connected to Maesflow microfluidic flow-control system (Fluigent), rinsed with TIRF buffer (10 mM imidazole [pH 7.4], 50 mM KCl, 1 mM MgCl$_2$, 1 mM EGTA, 0.2 mM ATP, 10 mM DTT, 15 mM glucose, 20 μg/mL catalase, 100 μg/mL glucose oxidase), and incubated with 1% BSA in TIRF buffer for 5 min. Spectrin-actin seeds were then passively adsorbed to the surface and used to nucleate actin filaments by then flowing in 1 μM actin monomers (15% Alexa 488 labeled) and 5 μM human Profilin-1. Thus, filaments were anchored at their pointed ends and grew at their distal free barbed ends to ∼5 μm in length. Next, 10 nM C-Daam2 polypetide (WT or p.Ser1027Leu) alone (no actin) was flowed in for 30 s to cap barbed ends. Then, the same G-actin-Profilin mix as above was flowed in, and barbed end actin filament elongation was monitored for 10–15 min.

All experiments were carried out at room temperature in TIRF buffer. Each experiment was repeated at least two times and yielded similar results. Time-lapse mf-TIRF imaging was performed using a Nikon-Ti200 inverted microscope equipped with a 150 mW Ar-Laser (Mellot Griot), a 60× TIRF-objective with a numerical aperture of 1.49 (Nikon Instruments), and an EMCCD camera (Andor Ixon). One pixel was equivalent to 143 × 143 nm. During measurements, optimal focus was maintained by the Perfect Focus system (Nikon Instruments).

Images were corrected for background fluorescence using the Fiji[58] rolling ball background subtraction algorithm (ball radius 5 pixels) and analyzed using the Fiji kymograph plugin, and the kymograph slopes were measured to determine the

depolymerization rates of individual filaments. One actin subunit was taken to contribute 2.7 nm to the filament length.

Pyrene-Actin Assembly Assay

Gel-filtered monomeric actin in G-buffer was cleared by ultracentrifugation for 1 h at 4°C at 350,000 × g in a TLA-100 rotor (Beckman Coulter), and the upper ~50% of the supernatant was carefully recovered and used for nucleation assays. All reactions (60 μL) contained 2 μM G-actin (10% pyrene labeled), which was converted to Mg^{2+}-ATP-actin 2 min before use. Then, 42 μL $Mg2^+$-ATP-G-actin was mixed rapidly with 15 μL proteins or control buffer and 3 μL of 20× initiation mix (40 mM $MgCl_2$, 10 mM ATP, and 1 M KCl) to initiate the reactions. Pyrene-actin fluorescence was monitored for 1,000 s using a fluorescence spectrophotometer (Photon Technology International) at excitation and emission wavelengths of 365 and 407 nm, respectively. The baselines of the resulting curves were corrected to each other and arbitrarily set to zero. The rate of actin assembly was determined from the slope of the curves over the first 500 s.

Xenopus Studies

Xenopus tropicalis were housed and cared for in our aquatics facility according to established protocols approved by Yale IACUC. We induced ovulation and collected embryos by *in vitro* fertilization as previously described.[59] Embryos were raised to stage 38 in 1/9MR + gentamycin. Staging of *Xenopus* tadpoles was performed according to Faber and Nieuwkoop.[60] CRISPR-Cas9-mediated genome editing in *Xenopus tropicalis* embryos was used as previously described.[61] A CRISPR sgRNA targeting a sequence encoding putative exon 7 of *daam2* was designed based on an available partial sequence (GenBank: XM_018090495.1) and its alignment against human and *Xenopus laevis* sequences was used to generate F0 knockout tissue in embryos (target sequence 5′-GGGCTACCGTTCCACTTATA-3′). For targeted loss-of-function experiments, 100 pg sgRNA along with 0.4 ng Cas9 (CP03, PNA Bio) in a 0.5 nL volume were injected into one cell of 4-cell stage embryos. In rescue experiments, 400 pg sgRNAalong with 1.6 ng Cas9 (CP03, PNA Bio) in a 2 nL volume were injected into 1-cell stage embryos followed by injection of 50 pg of mRNA in a 1 nL volume into one cell of 2-cell stage in the same embryos. Using the SP6 mMessage machine kit (Thermo Fisher) and following the manufacturer's instructions, we generated *in vitro* capped mRNA of wild-type and variant human *DAAM2* from sequences cloned into the pCSDest vector. mRNA was co-injected with a fluorescent tracer Mini-ruby (Thermo Fisher) in order to determine the injected side for subsequent analysis. We assessed the size of the pronephric region in stage 38 embryos corresponding to the proximal tubule by staining this structure with fluorescein labeled lectin (Vector Labs, FL-1141) as previously described.[62] Embryos were imaged on a Zeiss SteREO Lumar microscope. The size of the lectin stained structure was determined via uniform thresholding followed by automated particle analysis and area measurement utilizing Fiji.[63] Embryos with severe examples of the tissue bulging phenotypes were excluded from this analysis due to concerns that the bulges could obscure the tissue being visualized. We also assessed the effects of *daam2* knockout on cellular actin organization via staining with Alexa488 labeled phalloidin (Thermo Fisher). Actin was visualized through confocal microscopy carried out on a Zeiss LSM880. We detected *Xenopus tropicalis daam2* and *wt1* expression by generating digoxigenin-labeled antisense probes using the T7 High Yield RNA Synthesis kit (NEB, E2040S) and DIG-dUTP (Sigma) from cDNA derived amplified partial sequence for *daam2* (forward primer: 5′-ctcaaaactgccataatgtcctttatcaacgcc-3′; reverse T7 containing primer: 5′-ctagcTAATACGACTCACTATAG ccttcggtttgagttcctgatgttggga-3′) and *wt1* (forward primer: 5′-caca gctccccgatgctgtacaac-3′; reverse T7 containing primer: 5′-ctag cTAATACGACTCACTATAG cagtccctgcgtccctttgtctaaag-3′). Embryos were collected at stage 38 and fixed in MEMFA (1:1:8 10× MEMFA salts, 37% formaldehyde, distilled water) (10× MEMFA salts: 1 M MOPS, 20 mM EGTA, 10 mM $MgSO_4$) for 1–2 h at room temperature and dehydrated in 100% ethanol. Whole-mount *in situ* hybridization was done as previously described.[64] Rescue efficiency was assessed in the mRNA-injected side of embryos in which the contralateral side had *wt1* expression abnormalities. Successful rescue was based on the comparison between mRNA injected and mRNA un-injected sides with regard to *wt1* expression. Embryos were imaged with a Canon EOS 5d digital camera mounted on a Zeiss discovery V8 stereomicroscope. All experiments were performed a minimum of three times and numbers stated in graphs are the composite of multiple experiments.

Statistics

Statistical significance of abnormalities and rescues of proximal tubule size were evaluated using unpaired t tests. Percentages of embryos displaying *wt1* signal loss were evaluated using Fisher's exact tests. These statistical tests were carried out using GraphPad Prism v.8, GraphPadSoftware. In all figures, statistical significance was defined as p < 0.05. A single asterisk indicates p < 0.05, while double, triple, and quadruple asterisks indicate p < 0.005, p < 0.0005, and p < 0.0001, respectively. Paired t test was used to determine the statistical significance between two interventions. Standard deviation (SD) was used for all experiments other than for migration rate, where standard error of the mean was used (SEM).

Results

Bi-allelic Variants in *DAAM2* in Four Families with SRNS

In order to discover novel monogenic causes of steroid-resistant nephrotic syndrome (SRNS), we applied WES in individuals with SNRS in two centers for nephrogenic disorders in Boston and Munich. We identified five different bi-allelic variants in the formin-encoding gene *DAAM2* (GenBank: NM_015345.3) in four unrelated families with NS as follows: in family A3174, putative compound heterozygous missense variants c.361G>C (p.Glu121Gln) and c.1745C>A (p.Pro582His); in family B1068, a homozygous missense variant c.1004G>A (p.Arg335Gln); in family HN-F629, a homozygous nonsense variant c.1333C>T (p.Arg445*); and in family HN-F25, a homozygous missense variant c.3080C>T (p.Ser1027Leu) (Figures 1 and S1; Table 1). The respective altered amino acid residues are conserved to *D. melanogaster* (p.Arg335, p.Pro582, and p.Ser1027), and to *C. intestinalis* (p.Glu121) (Figure 1B, Table 1). With the exception of the heterozygous variant c.1745C>A, all variants are deemed likely disease causing by prediction programs, are absent homozygously, and are very rare heterozygously in the gnomAD database (Table 1). The missense variants are located in the N-terminal diaphanous-inhibitory-domain (DID, p.Arg335Gln), the

Table 1. Five Different Recessive Variants in *DAAM2* in Four Unrelated Individuals with Steroid-Resistant Nephrotic Syndrome

Family-Individual	Sex	Ethnic Origin	Nucleotide Change	Amino Acid Change	Exon (Zygosity, Segragation)	MT	PP2	CADD Score	Amino Acid Conser.	Frequencies in gnomAD Database (hom/het/total allele number)	Consanguinity	Age (years) of Onset (age at ESRD)	Renal Manifestation	Biopsy (at age)	Therapy and Response	Variant in Domain
A3174-21	M	Arabic	c.361G>C	p.Glu121Gln	5, het *	D	0.78	27.8	*C.i.*	0/1/238,766	no	2 (4)	SRNS	FSGS	steroids; no response	GBD
			c.1745C>A	p.Pro582His	14, het *	D	0.39	22.6	*D.r.*	1/436/279,340						FH1
B1068-21	M	Arabic	c.1004G>A	p.Arg335Gln	9, hom	D	1	32	*D.m.*	0/57/188,114	yes	5	SRNS	FSGS (?)	steroids; no response	DID
HN-F629	M	Turkish	c.1333C>T	p.Arg445*	12, hom	N/A	N/A	36	N/A	NP	yes	15 (33)	NS	FSGS	N/A	truncating
HN-F25	M	Arabic	c.3080C>T	p.Ser1027Leu	25, hom	D	0.8	27.7	*D.m.*	0/72/278,442	yes	8 (11)	SRNS	FSGS	steroids; no response	DAD

Abbreviations: CADD score, combined annotation dependent depletion; *C.i., Ciora intestinalis*; D, disease causing; DAD, diaphanous autoregulatory domain; DID, diaphanous inhibitory domain; *D.m., Drosophila melanogaster*; *D.r., Danio rerio*; ESRD, end-stage renal disease; FH, formin homology domain 1; FSGS, focal segmental glomerulosclerosis; GBD, GTPase Binding domain; gnomAD, genome aggregation database; het, heterozygous; hom, homozygous; M, male; N/A, not available; NP, not present; NS, nephrotic syndrome; PP2, PolyPhen-2 prediction score; MT variant taster prediction score. * Putative bi-allelic. Parental DNA was not available.

GTPase binding domain (GBD, p.Glu121Gln), formin-homology domain 1 (FH1, p.Pro582His), and the diaphanous-autoregulatory domain (DAD, p.Ser1027Leu) (Figures 1A and 1B). The nonsense variant identified in individual HN-F629 introduces a stop codon at position p.445 (Figures 1A and 1B) and is predicted to cause nonsense-mediated decay. Three families are of Arabic descent and one is of Turkish descent (Table 1). The homozygous variants were found in families reported to be of consanguinous union, while the compound heterozygous variants were found in an outbred family (Figures S1C and S1D). Homozygosity mapping suggested a recessive causative variant in the consanguinous families, and the causative variants are located within a homozygosity peak in chromosome 6 (Figure S1D). All individuals had nephrotic syndrome resistant to steroid treatment (documentation of response to treatment is lacking for individual HN-F629), with focal segmental glomerulosclerosis on histologic analysis of kidney biopsies and foot process effacement shown by electron microscopy (Figures 1D and 1E). None of the individuals had extra-renal manifestations of their disease, other than adrenal insufficiency in one individual (B1068_21) (Table 1). Renal ultrasound, when available, was characterized by increased cortical echogenicity (Figures 1C and 1F). Given the critical number of four families with five different likely deleterious bi-allelic variants, we conclude that bi-allelic variants in *DAAM2* may cause a monogenic form of human SRNS, which we suggest to be termed nephrotic syndrome type 22 (NPHS22).

DAAM2 Localizes to Renal Glomerular Podocytes and Interacts with INF2

Because most genes known to cause, when mutated, monogenic SRNS in humans are expressed in podocytes,[8–10] we analyzed the expression and localization of the *DAAM2* gene product in a human cultured podocyte cell line. Immunofluorescence revealed expression of *DAAM2* in cultured podocytes (Figures S2D, S2H, S2I, and S8). DAAM2 was also detected in murine glomerular podocytes and partially co-localized with nephrin and with Inverted Formin 2 (INF2), and to a lesser extent with synaptopodin and actinin-α4 (Figures 2A–2D). Using immunohistochemistry, we also immunolocalized DAAM2 to the glomerulus of human kidney, in a pattern suggesting podocyte localization (Figure 2E). This observation agrees with data published in the human protein atlas database and with recently published single-cell RNA sequencing databases (scRNA-seq).[8–10]

Variants in *INF2* cause monogenic SRNS/FSGS.[30] INF2 not only directly promotes actin assembly, but also binds to other formins and controls their ability to regulate actin assembly.[45] Based on available scRNA-seq data, INF2 is highly expressed in podocytes.[8] We therefore hypothesized that DAAM2 and INF2 may molecularly interact. To test this model, we performed coimmunoprecipitation in cultured human embryonic kidney cells (HEK293T) and found that DAAM2 and INF2 co-immunoprecipitated
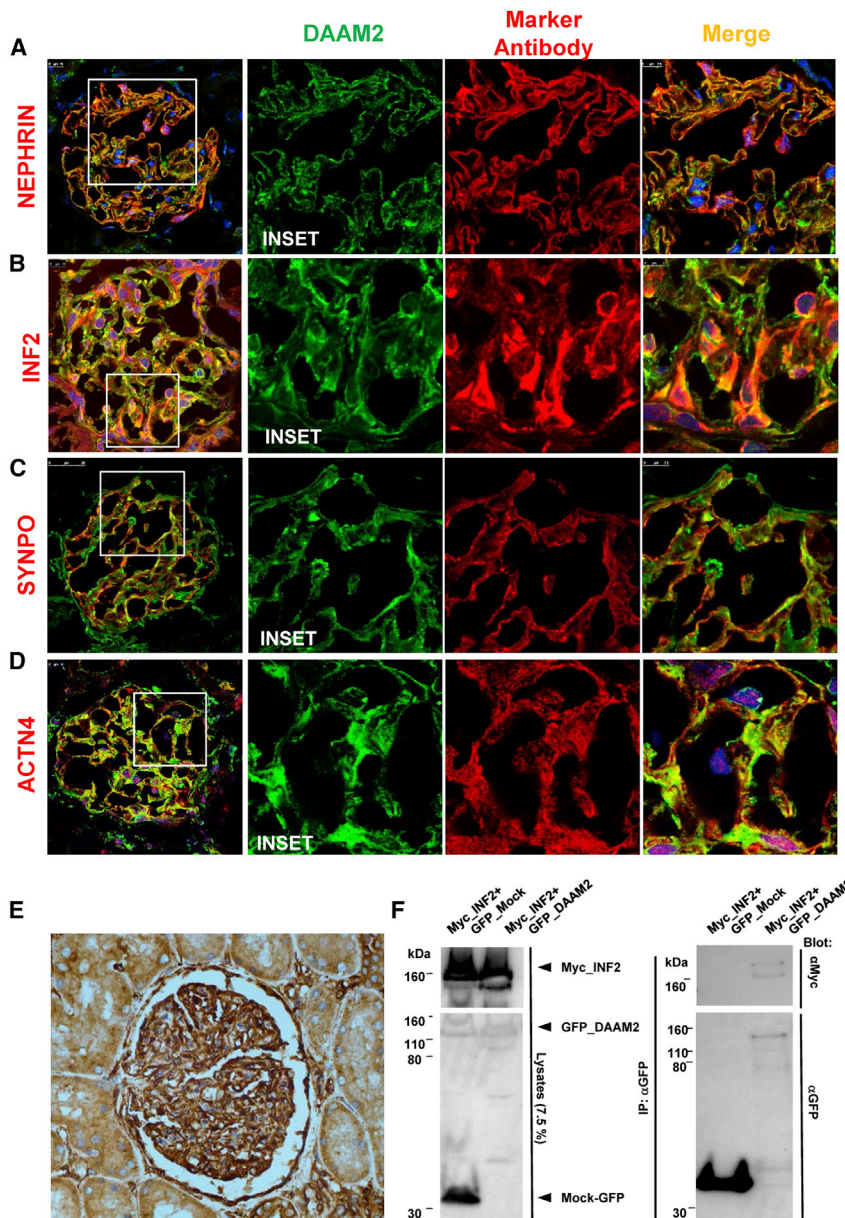
Figure 2. DAAM2 Partially Co-localizes with Nephrin and INF2 to Human and Rat Glomerular Podocytes

(A–D) Immunofluorescence staining shows that DAAM2 localizes to podocytes in rat glomeruli and partially co-localizes with (A) nephrin, and (B) Inverted Formin 2 (INF2) but to a lesser extent with (C) synaptopodin (SYNPO) or (D) actinin-alpha-4 (ACTN4).

(E) Immunohistochemistry (IHC) staining using specific custom-made anti-DAAM2 antibody (Boston molecules) shows DAAM2 to localize to healthy human kidney glomeruli, in a pattern strongly suggestive of podocyte localization.

(F) GFP_DAAM2 but not GFP_Mock co-precipitates Myc_INF2 using a co-immunoprecipitation assay (Co-IP) in HEK293T cells.

(Figures 2F, S2L, and S8). These results suggest that DAAM2 and INF2, of which variants are both implicated in monogenic nephrotic syndrome, physically interact and colocalize in rat glomerular podocytes.

Mutant DAAM2 Impairs Filopodia Formation in Podocytes

Since formins are known to act downstream of small GTPases to induce actin polymerization and filopodia formation[65] (Figure S8), we hypothesized that wild-type DAAM2, but not SRNS-derived mutants, might promote filopodia formation. Using fluorescent live imaging, we found that GFP-tagged wild-type DAAM2 overexpression in a human podocyte cell line increased filopodia format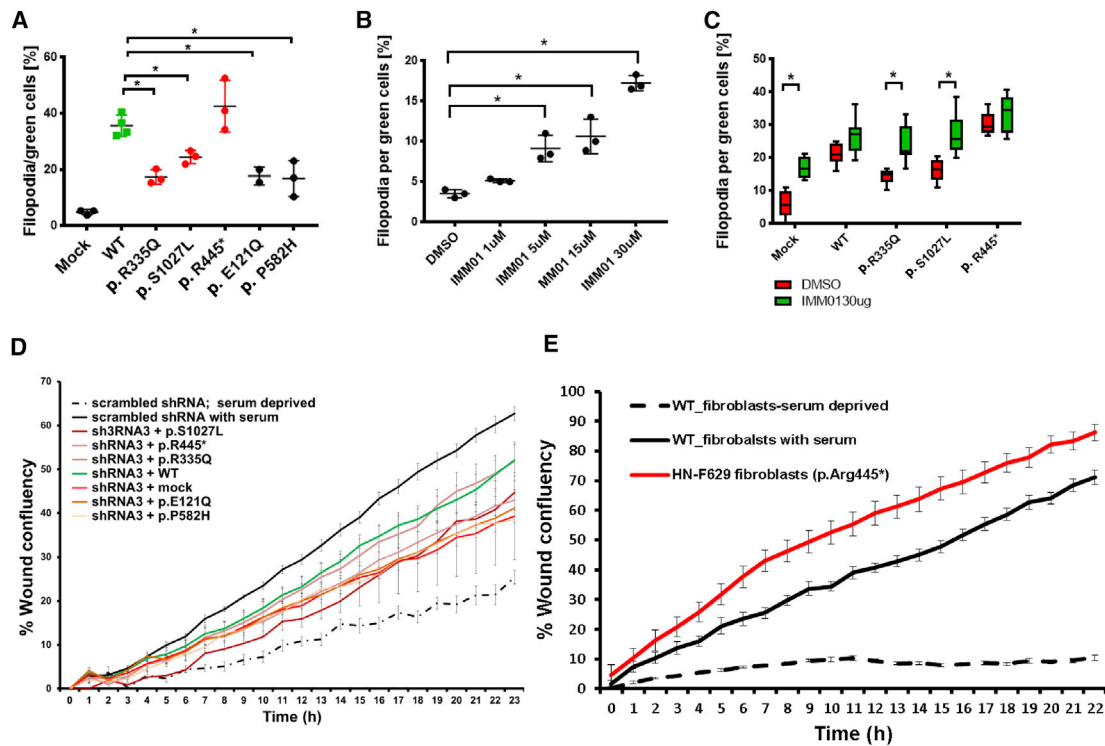ion, defined as 2 or more filopodia per cell, to a higher degree (32%–40.5%) in GFP-positive podocytes, than overexpression of cDNAs carrying the 4 human missense variants (15.3%–26.67%) (Figures 3A and S8). In contrast, less than 5.5% of GFP-Mock overexpressing control cells showed filopodia formation. Interestingly, overexpressing cDNA representing the early truncating variant p.Arg445* induced filopodia to a similar range as WT-DAAM2 (34.2%–52.5%) (Figures 3A and S3J–S3K). We conclude that this aspect of actin cytoskeleton remodeling, to form filopodia, is impaired by DAAM2-SRNS missense variants.

Because formins are autoinhibited via intramoleculaar DID-DAD interactions, we hypothesized that pharmacologic formin activation might rescue the loss of filopodia formation induced by knockdown of DAAM2 or expression of mutant DAAM2 (Figure S8). The formin agonist Intramimic-1 (IMM-01)[66] acts by disrupting the autoinhibitory bond between the DID and DAD domain and thus activates formins. To test this hypothesis, we generated a DAAM2-deficient human podocyte cell line by shRNA knockdown (Figure S3D) and applied IMM-01 in increasing doses of 1 to 30 μM to the DAAM2 knockdown (k.d.) cells. We observed an increase in filopodia formation from 4% in cells treated with control vehicle only (DMSO) to 15%–18% in cells treated with 30 μM IMM-01 (Figure 3B). Next, we overexpressed cDNA representing variants derived from individuals with SRNS in DAAM2 k.d. cells and then treated these cells with 30 μM IMM-01. This resulted in rescue of filopodia formation in cells with DAAM2 k.d. expressing DAAM2-missense mutants. In contrast, cells expressing wild-type DAAM2 or p.Arg445*

Figure 3. *DAAM2* Regulates Podocyte Migration Rate and Filopodia Formation in Human Podocyte Cell Line

(A) Overexpression of GFP-tagged cDNA clones representing WT-DAAM2 in a human podocyte cell line, induced filopodia formation to a significantly higher extent than overexpressing cDNA that represent the missense variants p.Glu121Gln, p.Arg335Gln, p.Pro582His, and p.Ser1027Leu derived from individuals with SRNS. Overexpressing p.Arg445* cDNA resulted in high rate of filopodia formation, comparable to WT-DAAM2. Each dot represents an independent experiment for which at least 100 transfected (green fluorescent) cells have been counted and assessed for filopodia formation, for each condition. Filopodia forming cell was defined as cell exhibiting two or more cellular protrusions (see Figures S3J–S3M). *p < 0.05 (one-way ANOVA).

(B) Applying the formin-activating small molecule intramimic-1 (IMM-01) induced filopodia formation in shRNA *DAAM2*-k.d. human podocyte cell line in a dose-dependent manner. Each dot represents an independent experiment for which at least 100 podocytes were assessed for filopodia formation for each IMM01 dose.

(C) In a *DAAM2*-k.d. human podocyte cell line, overexpression of WT-DAAM2 cDNA fully rescued filopodia formation, while overexpression of cDNA representing human SRNS variants p.Arg335Gln and p.Ser1027Leu resulted only in partial rescue. Applying IMM-01 fully rescued filopodia formation. IMM-01 administration did not significantly change filopodia formation in cells overexpressing WT-DAAM2 or the mutant p.Arg445*. 16 (X10) fields were evaluated for filopodia formation in transfected cells/condition (> 100 cells per condition).

Error bars represent standard deviation (SD) in (A)–(C).

(D) Podocyte migration rate (PMR) is analyzed by the IncuCyte videomicroscopy and Zoom software. As negative control we use wild-type cells treated with scrambled shRNA, plated in the absence of serum. As positive control we plate the same cells but with the presence of serum. All other conditions are with serum as well. *DAAM2* knockdown by shRNA decrease PMR. The decrease in PMR was partially rescued by transfection of mouse WT-*Daam2* and by cDNA representing p.Arg445* variant, but was not rescued by murine *DAAM2* constructs reflecting SRNS-causing missense variants. Each experiment was conducted three times, with ten repeats/condition in each experiment. Error bars = SEM.

(E) Fibroblasts cultured from a skin biopsy from individual HN-F629 (variant p.Arg445*) migrate faster than healthy control skin fibroblasts in the migration assay. Error bars = SEM; n = 3 experiments, 30 repeats/condition in each experiment.

showed increased filopodia formation, with no further increase after IMM-01 administration (Figure 3C). We conclude that relieving formin auto-inhibition can rescue deficient DAAM2 activity and induce filopodia formation.

DAAM2 Missense Variants Fail to Rescue Defects in Podocyte Migration Rate

Because of our observations above showing that DAAM2 affects podocyte actin organization, we tested the possibility that DAAM2 might also regulate podocyte migration rate (PMR), which is modulated by actin regulators encoded by genes of which variants cause monogenic SRNS[16,17,25,53,54] (Figure S8). To test this hypothesis, we induced a *DAAM2* knockdown in cultured podocytes using shRNA and confirmed successful *DAAM2* knockdown by immunoblotting (Figure S3D). We generated a standardized scratch in a monolayer of these cells and monitored podocyte migration using the IncuCyte videomicroscopy system over time. Two independent shRNA lines showed reduced PMR (Figure S3A). To test whether the slowdown is specific to the DAAM2 knockdown, we transiently expressed an RNAi-refractive murine wild-type *Daam2*

cDNA rescue construct and observed partial reversal of the reduced migration rate. This suggests a role for DAAM2 in supporting normal podocyte migration. Expression of murine mRNA constructs reflecting the missense variants p.Glu121Gln, p.Arg335Gln, p.Pro582His, and p.Ser1027-Leu from individuals with SRNS failed to rescue PMR (Figures 3D, S3B, and S3C). This indicates that DAAM2 dysfunction due to SRNS-related missense variants leads to impaired podocyte migration. Paradoxically, overexpression of p.Arg445* mutant fully rescued PMR (Figure S3B).

Since overexpression of the nonsense variant p.Arg445* paradoxically promoted filopodia formation and cell migration, we further examined the migration rate for this mutant by using the migration rate assay in a fibroblast cell line derived from individual's HN-F629 skin biopsy. We confirmed the presence of the nonsense variant in this individual-derived cell line by Sanger sequencing (Figure S3E) and the absence of a band corresponding to DAAM2 on western blot (Figures S3G–S3I). We applied a scratch to a monolayer of cells and compared the fibroblast migration rate (FMR) for this cell line with a control primary skin-fibroblast cell line from a healthy human. We observed a faster cell migration for the cells deficient in DAAM2 (bearing the mutant p.Arg445*) compared to WT controls (>20 wells/condition in each experiment, n = 3) (Figures 3E and S3F). We conclude that actin remodeling is impaired by *DAAM2* SRNS-missense variants as reflected in podocyte migration, and that overexpressing the N-terminal part of DAAM2, or the absence of DAAM2, result in fast migration of cells.

DAAM2 Variants Have Altered Effects on Actin Assembly In Vitro

To address whether *DAAM2* variants linked to NS might have altered effects on actin filament nucleation and/or elongation *in vitro*, we purified the N- and C-terminal halves of DAAM2 corresponding to the wild type (WT) or the p.Arg335Gln and p.Ser1027Leu variant sequences (Figure 4A). Interestingly, the p.Arg335Gln variant is located in the DID region, and the p.Ser1027Leu variant is located in the DAD region (Figures 1A and 1B). This suggests that either or both variants might alter DAAM2 autoregulation. However, DAD-containing C-terminal tail regions also bind to actin and enhance FH2-mediated actin nucleation and processive elongation.[67,68] Thus, the p.Ser1027Leu variant could influence not only auto-inhibition, but also actin nucleation and/or elongation.

We first compared the C-DAAM2 polypeptides for their actin nucleation effects in bulk pyrene-actin assembly assays (Figure 4B). Similar to the effects of other formins in these biochemical assays,[31,41,68,69] C-DAAM2 (WT) stimulated actin assembly. This represents a demonstration of DAAM2's actin assembly-promoting capabilities, which are roughly similar in their potency to those of Daam1.[31,69] Thus, both members of this formin subfamily, DAAM1 and DAAM2, directly stimulate actin nucleation.

To our surprise, the p.Ser1027Leu variant of C-DaamAAM2 promoted actin nucleation even more efficiently than WT C-DAAM2, and did so over a wide concentration range (Figures 4C, S4A, and S4B). The primary activity monitored in the bulk assays (by the increase in pyrene fluorescence) is actin nucleation, not elongation.[70] Thus, our results suggest that the p.Ser1027Leu variant has aberrantly strong nucleation activity compared to WT C-DAAM2.

To directly evaluate the effects of C-DAAM2 polypeptides on actin filament elongation rate, we employed microfluidic-assisted total internal reflection fluorescence (mf-TIRF) microscopy[54,71] (see schematic in Figure S4C). This technique allows accurate quantitative analysis of changes in filament length over time and enables one to rapidly introduce or exchange reaction ingredients.[54,71] Spectrin-actin seeds are anchored to the viewing surface and used to polymerize actin filaments that grow at their free barbed ends. Kymographs reveal change in filament length over time, and the rate of elongation is derived from the slope (see dotted line, Figure 4D). In the presence of profilin, WT C-DAAM2 polypeptide accelerated barbed end growth by almost 5-fold compared to control reactions lacking C-DAAM2 (WT C-Daam2: 33 ± 10 actin subunits* s^{-1}*μM^{-1}; control: 7 ± 1 actin subunits*s^{-1}*μM^{-1}) (Figure 4E). This is slightly faster than the rate of elongation supported by Daam1.[69] Interestingly, the p.Ser1027-Leu variant of C-DAAM2 supported a significantly slower rate of elongation (22 ± 5 actin subunits*s^{-1}*μM^{-1}), intermediate between WT C-DAAM2 and control. Thus, while the p.Ser1027Leu variant C-DAAM2 enhances actin nucleation activity, it also reduces the rate of filament elongation compared to WT C-DAAM2.

We next investigated the effects of the variants on formin auto-inhibition. In bulk assays, the N-terminal halves of formins can inhibit the actin assembly activities of the C-terminal halves in *trans*, as previously demonstrated for Dia1 and Daam1.[31,41] We compared the abilities of different concentrations of WT N-DAAM2 to inhibit the actin assembly activities of WT and p.Ser1027Leu variant C-DAAM2. Inhibition was stronger for p.Ser1027Leu C-DAAM2 compared to WT C-DAAM2 (Figures 4F and S4E–S4G), suggesting that the p.Ser1027Leu variant aberrantly strengthens DID-DAD interactions. Next, we compared the effects of WT and p.Arg335Gln N-DAAM2 at a range of concentrations on the actin assembly activity of WT C-DAAM2 (Figure S4D–S4F), which revealed enhanced inhibition by the p.Arg335Gln variant of N-DAAM2 compared to WT N-DAAM2. Thus, both NS variants (p.Arg335Gln and p.Ser1027Leu) enhanced DID-DAD auto-inhibition.

It is worth noting that DAAM2 autoinhibitory effects are relatively weak compared to some other formins (IC_{50} approximately two orders of magnitude higher than Dia1[31,41]) and saturated at ~50% inhibition. Therefore, WT DAAM2 may be only weakly regulated by classic DID-DAD interactions, and possibly requires other cellular factors to achieve tight inhibition, as recently
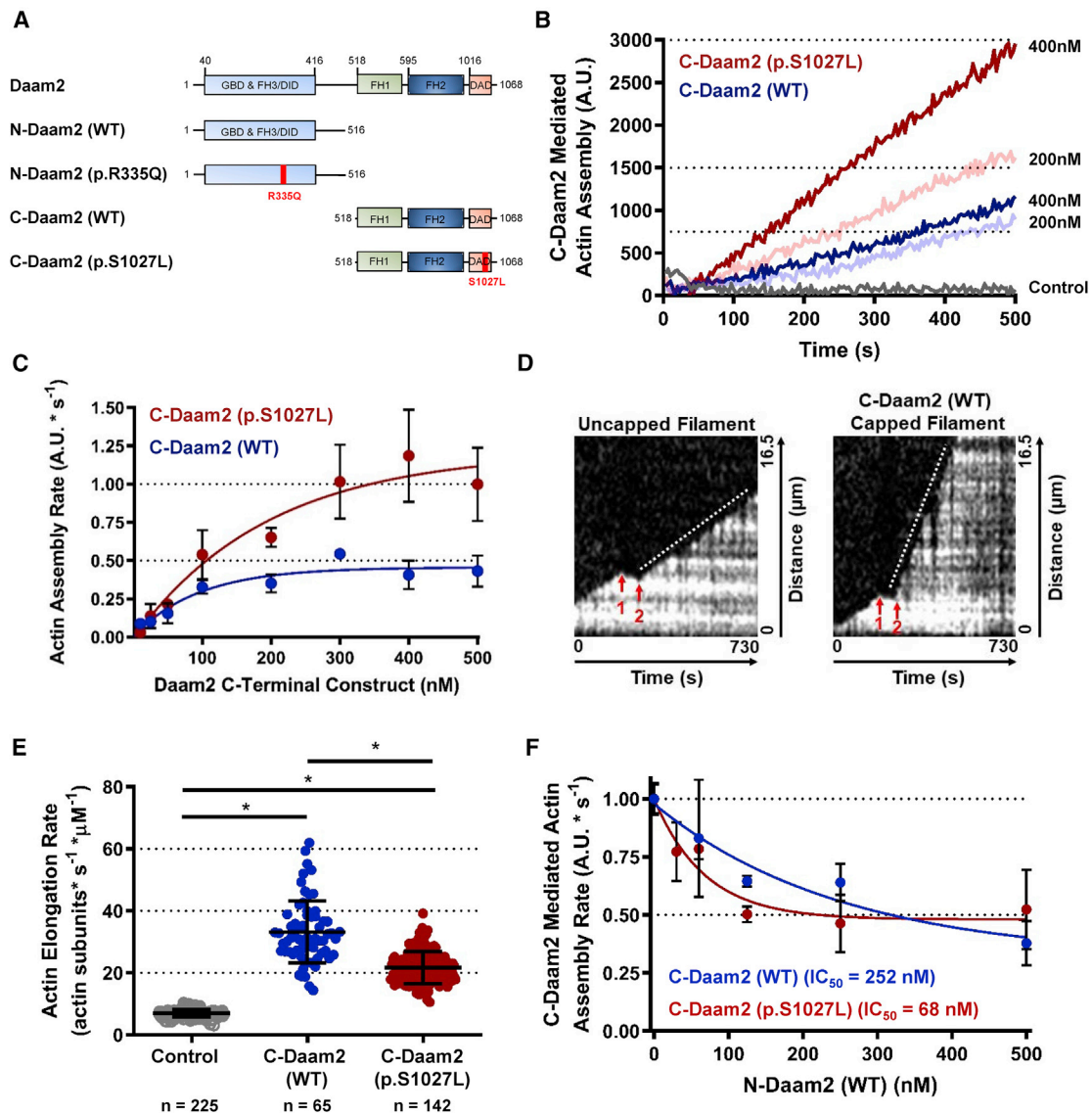
Figure 4. *DAAM2* **Variants Influence Actin Nucleation and Elongation Rates**

(A) Domain structure of Daam2 and the specific constructs that were biochemically characterized in this study. GBD, GTPase binding domain; FH3, formin homology 3; DID, diaphanous inhibitory domain; FH1, formin homology 1; FH2, formin homology 2; DAD, diaphanous autoregulatory domain. Positions of variants (p.Arg335Gln and p.Ser1027Leu) are indicated in red.

(B) Bulk actin assembly assays comparing the effects of different concentrations of C-Daam2 (WT) and C-Daam2 (p.Ser1027Leu) on the polymerization of 2 μM G-actin (10% pyrene labeled) in the presence of 5 μM profilin. Increase in fluorescence corresponds to increase in actin assembly into filaments.

(C) Quantification of data from bulk assays as in (B). The data show that C-Daam2 (p.Ser1027Leu) variant promotes actin assembly more effectively than C-Daam2 (WT), suggesting that the variant has aberrantly strong nucleation activity.

(D) Example kymographs for two different filaments from the same microfluidic-assisted TIRF (mf-TIRF) microscopy assay, monitoring elongation of barbed ends over time. Filaments are initially grown in the presence of 1 μM G-actin (15% Alexa 488 G-actin) and 5 μM profilin. Arrow 1 indicates when 10 nM C-Daam2 (WT or p.Ser1027Leu) was flowed into the reaction (without actin or profilin) to cap some of the barbed ends. This led to a 30 s interruption of growth. Arrow 2 indicates when actin monomers and profilin were reintroduced to allow growth to resume. The kymograph on the left shows an uncapped barbed end elongating at a slower rate, and the kymograph on the right shows a C-Daam2 (WT) capped filament elongating at an accelerated rate. Dotted lines highlight the regions of the kymograph used to measure the slopes (rate of elongation).

(E) Quantification of data from mf-TIRF assays as in (D), pooled from two independent experiments. Each data point represents the elongation rate of a single filament measured for 5–8 min.

(F) Quantification of bulk assays as in (B), comparing the inhibitory effects of N-Daam2 (WT) on the actin assembly activity of C-Daam2 (WT) and C-Daam2 (p.Ser1027Leu). The data show that the N-Daam2 (WT) is more effective in inhibiting C-Daam2 (p.Ser1027Leu) than C-Daam2 (WT). Also see Figure S4 for a comparison of the inhibitory effects of N-Daam2 (WT) and N-Daam2 (p.Arg335Gln) on the activity of C-Daam2 (WT). All experiments were performed twice.

For (B), the data shown are from one representative experiment. For all other panels, the data were averaged. Error bars represent SD. * represents statistical significance at $p \geq 0.05$ with Student's t test.
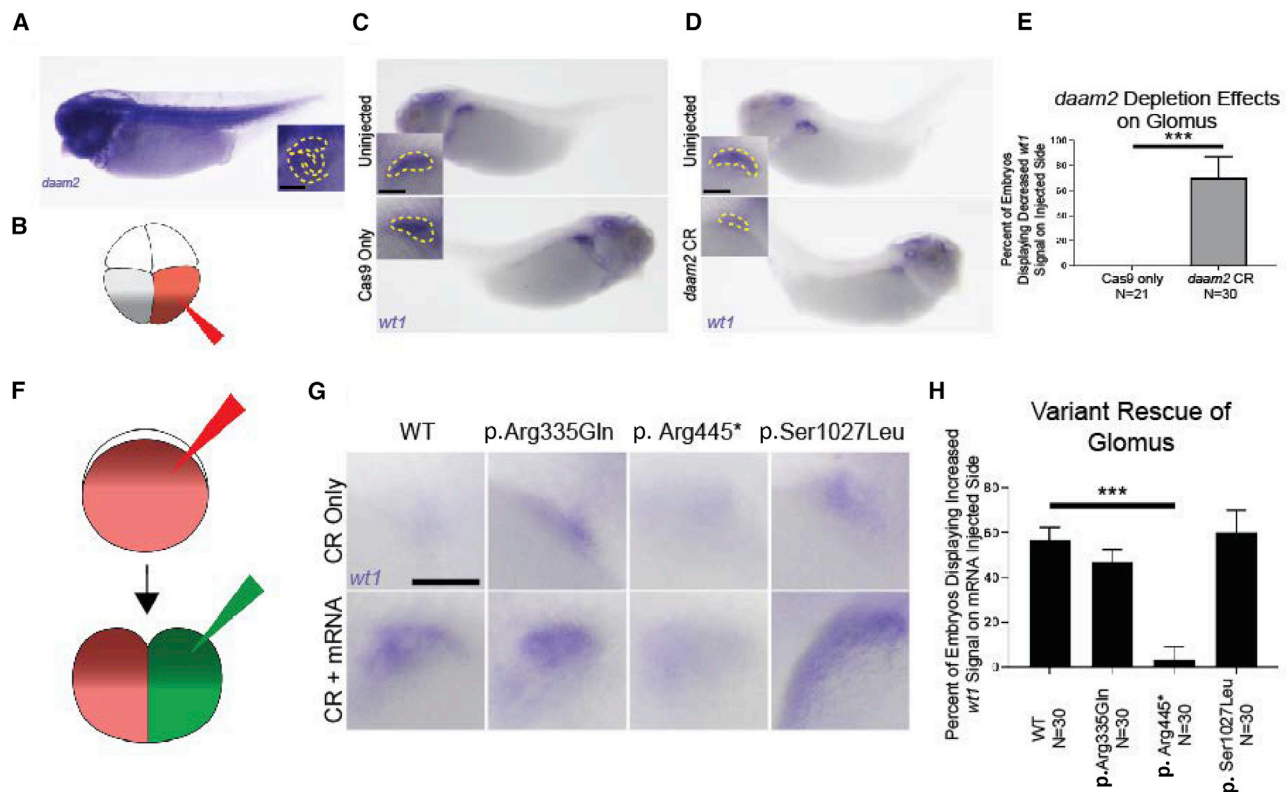
Figure 5. *DAAM2* Knockout in *Xenopus* Results in Glomerular Maldevelopment

Xenopus embryos were injected with Cas9 and CRISPR guide RNA (gRNA) oligonucleotides targeting *daam2* in one cell at the 4-cell stage. Percent of embryos displaying glomerular maldevelopment was calculated. The glomus was detected using whole-mount *in situ* hybridization for *wt1* as a marker.

(A) Whole-mount *in situ* hybridization for *daam2* revealed strong expression in the head, neural tube, and the pronephric region.

(B) Schematic of the knockdown experimental setup.

(C) Control embryo, uninjected (upper left panel), or injected with Cas9 (lower left panel) displaying appropriate glomerular development. Mosaic k.o. of *daam2* results in abnormalities of glomus development (injected side: lower right, uninjected: upper right panel).

(D) Percent of embryos displaying decreased wt1 signal on injected side.

(E) Injection of wild-type human mRNA of *DAAM2* restores wt1 signal as a marker of restored glomus development. Injection of mRNA reflecting variants p.Arg335Gln and p.Ser1027Leu from individuals with NS also restores *wt1* signal, but injection of mRNA reflecting p.Arg445* mutant fails to do so.

(F) Percent of embryos displaying increased *wt1* signal on mRNA-injected side is shown for WT and mutant mRNA injection. ***p < 0.0005 by Fisher's exact test. Scale bars depict 100 μm.

demonstrated for the formin INF2.[72] We also attempted to isolate the DAAM2 p.Arg445* variant (an early stop codon), which encodes a polypeptide containing amino acids 1–444; however, this construct was insoluble. In summary, we conclude that *in vitro* actin nucleation, actin assembly, and autoregulatory functions of DAAM2 are impaired by the DAD and DID domain SRNS variants p.Arg335Gln and p.Ser1027Leu (Figure S8).

Knockout of *daam2* in *Xenopus tropicalis* by CRISPR-Cas9 Results in Glomerular Maldevelopment

We determined that *WNT* might serve as a model for *DAAM2* variant kidney disease based on observed expression of *daam2* in the pronephric region of developing embryos (Figure 5A). At the 4-cell stage, *Xenopus* embryos were injected with Cas9 along with an sgRNA targeting *daam2*. While one side of the embryo featured a pronephros and glomus that developed from an un-injected cell

and served as an internal control, the contralateral pronephros and glomus developed from the injected cell (Figure 5B). At stage 38, *in situ* hybridization for expression of the glomus marker *wt1* was used to assess defects in this tissue due to *daam2* knockout. Compared to control tissue within the embryos, tissue with knockout of *daam2* demonstrated a loss of *wt1* signal (Figures 5C–5E). Quantification of lectin staining revealed a significant decrease in the ratio of proximal tubule area between knockout and control pronephric tissues (Figures S5A and S5B).

In the course of carrying out *daam2* knockout experiments to assess embryonic kidney tissue, we observed that developing tadpoles frequently developed bulging tissue within regions subject to gene knockout. To assess the underlying cellular organization that could be giving rise to this phenotype, we examined F-actin staining in the tissue bulges and found cells with abnormally variable size and abnormally distributed F-actin (Figures S6A and S6B).

To assess both the specificity of our knockout and the functionality of *DAAM2* variants discovered in individuals with SRNS, we employed rescue experiments. We first injected Cas9 and *daam2* sgRNA at the 1-cell stage to deplete these proteins throughout the embryo. Then, at the 2-cell stage, we injected one cell of these morphants with wild-type human mRNA of *DAAM2*. In this manner, we could internally compare loss-of-function and rescued kidney tissue for differences in morphology (Figure 5F). As expected, wild-type *DAAM2* mRNA rescued the abnormal kidney morphology seen in knockout tissue (Figures 5G, 5H, S5C, and S5D); in contrast, injection of mutant *DAAM2* mRNA resulted in impaired restoration of proximal tubule area (Figures S5C and S5D). With respect to the ability to restore *wt1* signal found within the glomus, the variants displayed a range of rescue efficacy. While mRNA from the p.Arg335Gln and p.Ser1027Leu variants seemed to restore *wt1* signal in the glomus, the p.Arg445* variant did not (Figures 5G and 5H). Interestingly, the rescue of *wt1* expression achieved via the introduction of the p.Ser1027Leu variant consistently led to an expanded *wt1* signal, suggesting the persistence of tissue dysmorphology despite the ability to rescue glomus marker expression.

In summary, we discovered variants of *DAAM2* as possible monogenic causes of nephrotic syndrome, and our findings confirm actin formation and regulation by formins as a critical pathomechanism in human SRNS.

Discussion

Here, we describe the discovery of bi-allelic variants in *DAAM2* as likely monogenic causes of SRNS in four distinct families with SRNS. We generated a set of testable hypotheses summarized in Figure S8. We found that the DAAM2 protein localizes to glomerular podocytes. We demonstrated that DAAM2 is an interaction partner of the formin family member INF2, variants in which lead to autosomal-dominant human SRNS. Further, we found that DAAM2 and INF2 colocalize in adult rat glomeruli. To the best of our knowledge, INF2 and DAAM2 interaction was not described in the past and hence the specific interacting domains are unknown. However, the N-terminal DID domain of INF2 was described to interact with the C-terminal DAD domain of other formins, the diaphanous-related formins, which have a very similar domain structure to DAAM2.[45] Whether DAAM2 interacts with INF2 through its C-terminal DAD domain as well should be tested in a future work.

Prior studies using mouse and *in vitro* models have explored the role of DAAM2 in the WNT pathway. In these studies, DAAM2 was found to be a WNT effector, acting downstream of WNT to modulate dorsal patterning through interaction with dvl3,[73] playing a role in generation of left-right asymmetry during organ development through regulation of the actin cytoskeleton,[74] and play-

ing a key role in axon formation[75] and myocardial development (together with DAAM1) through Rho activation.[76] Since regulation of the actin cytoskeleton through Rho/Rac1/CDC42 is crucial for podocyte function, we hypothesized that variants in DAAM2 are deleterious through effects on actin assembly dysregulation.

Using *in vitro* and *in vivo* assays, we provide evidence for loss-of-function caused by the *DAAM2* variants in bulk actin assembly and TIRF microscopy assays, C-DAAM2 (WT) promoted actin nucleation and elongation, and these activities were impaired by the individual-derived variants p.Arg335Gln and p.Ser1027Leu, indicating a loss-of-function mechanism by affecting essential positions in either the DID or DAD domains. In cultured podocytes, SRNS individual-derived missense variants reduced "filopodia formation" and "podocyte migration" rate. These effects could be partially rescued by treating cells with the formin activator IMM-01, demonstrating the importance of formins in podocyte cytoskeletal regulation. Finally, in a *Xenopus daam2* knockout model, we showed that daam2 is critical for cellular F-actin organization and for glomerular development, a phenotype that could be rescued with wild-type *daam2* mRNA but not with mRNA representing the nonsense mutant p.Arg445*. We conclude that *DAAM2* variants are a likely cause of monogenic human SRNS, due to actin dysregulation in podocytes. Further, we provide evidence that this variant of SRNS may be amenable to treatment with actin-regulating compounds.

Individual HN-F629 was unusual in his clinical presentation because his nephrotic syndrome presented late, having developed ESRD only in the 4th decade of life. Interestingly, he is the only individual among the four affected individuals who carries a truncating variant (p.Arg445*). When the functional effects of p.Arg445* were studied, two of the assays conducted in cultured podocytes, filopodia formation and migration, showed paradoxical rescue of loss-of-function phenotype when mRNA mutant cDNA representing p.Arg445* from individual HN-F629 was overexpressed, whereas expression of the missense variants p.Glu121Gln, p.Arg335Gln, p.Pro582His, and p.Ser1027-Leu had the opposite effect. Furthermore, migration of skin fibroblasts derived from this individual paradoxically showed faster migration compared to control fibroblasts. In contrast, in the *Xenopus* model expressing p.Arg445* cDNA did not rescue the glomus maldevelopment of daam2 knockout animals, whereas p.Arg335Gln and p.Ser1027Leu mutants did rescue to a variable degree. These results could perhaps be explained by an "escape" from inhibition, arising from loss of the C-terminal half of DAAM2. In other words, the defects caused by the other point mutants only manifest in the presence of the C-terminal half of DAAM2. Interestingly, an independent inhibitory role for the N-terminal part of INF2 on DIAPH1 in podocytes was recently demonstrated.[77] Our findings of interaction between INF2 and DAAM2 may suggest loss of inhibition by INF2 on DAAM2-p.Arg445* in a similar manner. Alternatively, a nonsense-mediated-decay (NMD)-

dependent compensatory mechanism could potentially explain a milder phenotype in this individual.[78] In conclusion, the functional effects of missense variants showed reductions in filopodia formation, reductions in podocyte migration rate, and variable rescue in the *Xenopus* daam2 knockout model, whereas the p.Arg445* truncating variant had opposite effects throughout. Interestingly, the phenotype of the individual with the truncating variant also differed strongly, by showing very late onset of NS. This may indicate that different types of variants in DAAM2 have the capacity to alter cellular actin regulation in different ways, ultimately leading to variation in the timing and severity of SRNS phenotypes as was described in Warejko et al.[6]

We screened a cohort of ~2,100 individuals with nephrotic syndrome by WES but did not identify additional individuals with variants in *DAAM2*. *DAAM2* variants thus appear to be a rare cause of SRNS.[5] This is consistent with most of the recently discovered monogenic causes of nephrotic syndrome. Nevertheless, the identification of numerous monogenic causes of NS which are directly involved in actin cytoskeleton regulation in podocytes has shaped our understanding of the central role of actin in podocyte physiology and SRNS. Moreover, the convergence of multiple pathways involved in monogenic NS on actin regulation holds promise for successful therapeutic intervention by pharmacological modulation of actin.

While variants in the DID domain of the formin *INF2* were reported to cause autosomal-dominant isolated SRNS or associated with Charcot-Marie-Tooth syndrome (MIM: 614455),[79] we describe here SRNS causing variants in another formin (*DAAM2*). Our findings thus reveal variants in the formin-encoding gene *DAAM2* as likely monogenic causes of SRNS and suggest that actin regulation by *DAAM2* is an important pathomechanism of human SRNS.

Data and Code Availability

The datasets supporting the current study have not been deposited in a public repository due to restriction by patient consent, but are available from the corresponding author on request. Human *DAAM2* full-length gene is GenBank: NM_015345.3 and UniProt protein ID: Q86T65. Mouse *DAAM2* full-length protein is UniProt: Q80U19. *Xenopus* Xenbase: XB-GENE-6049503.

Supplemental Data

Supplemental Data can be found online at https://doi.org/10.1016/j.ajhg.2020.11.008.

Acknowledgments

Declaration of Interests

F.H. is a cofounder and SAB of Goldfinch-Bio. The other authors declare that they have no competing financial interests.

Web Resources

GenBank, https://www.ncbi.nlm.nih.gov/genbank/
GraphPad, https://www.graphpad.com/
Ensembl Genome Browser, http://www.ensembl.org
gnomAD browser beta, https://gnomad.broadinstitute.org/
MutationTaster http://www.mutationtaster.org
OMIM, https://www.omim.org/
PolyPhen2, http://genetics.bwh.harvard.edu/pph2
Renal Genes, http://www.renalgenes.org
Sorting Intolerant From Tolerant (SIFT), http://sift.jcvi.org
UCSC Genome Browser, https://genome.ucsc.edu
UniProt, http://www.uniprot.org/
Xenbase, http://www.xenbase.org/entry/

References

1. Vivante, A., and Hildebrandt, F. (2016). Exploring the genetic basis of early-onset chronic kidney disease. Nat. Rev. Nephrol. *12*, 133–146.

2. Tan, W., Lovric, S., Ashraf, S., Rao, J., Schapiro, D., Airik, M., Shril, S., Gee, H.Y., Baum, M., Daouk, G., et al. (2018). Analysis of 24 genes reveals a monogenic cause in 11.1% of cases with steroid-resistant nephrotic syndrome at a single center. Pediatr. Nephrol. *33*, 305–314.

3. Lovric, S., Ashraf, S., Tan, W., and Hildebrandt, F. (2016). Genetic testing in steroid-resistant nephrotic syndrome: when and how? Nephrol. Dial. Transplant. *31*, 1802–1813.

4. Lovric, S., Fang, H., Vega-Warner, V., Sadowski, C.E., Gee, H.Y., Halbritter, J., Ashraf, S., Saisawat, P., Soliman, N.A., Kari, J.A., et al.; Nephrotic Syndrome Study Group (2014). Rapid detection of monogenic causes of childhood-onset steroid-resistant nephrotic syndrome. Clin. J. Am. Soc. Nephrol. *9*, 1109–1116.

5. Sadowski, C.E., Lovric, S., Ashraf, S., Pabst, W.L., Gee, H.Y., Kohl, S., Engelmann, S., Vega-Warner, V., Fang, H., Halbritter, J., et al.; SRNS Study Group (2015). A single-gene cause in 29.5% of cases of steroid-resistant nephrotic syndrome. J. Am. Soc. Nephrol. *26*, 1279–1289.

6. Warejko, J.K., Tan, W., Daga, A., Schapiro, D., Lawson, J.A., Shril, S., Lovric, S., Ashraf, S., Rao, J., Hermle, T., et al. (2018). Whole Exome Sequencing of Patients with Steroid-Resistant Nephrotic Syndrome. Clin. J. Am. Soc. Nephrol. *13*, 53–62.

7. Landini, S., Mazzinghi, B., Becherucci, F., Allinovi, M., Provenzano, A., Palazzo, V., Ravaglia, F., Artuso, R., Bosi, E., Stagi, S., et al. (2020). Reverse Phenotyping after Whole-Exome Sequencing in Steroid-Resistant Nephrotic Syndrome. Clin. J. Am. Soc. Nephrol. *15*, 89–100.

8. Karaiskos, N., Rahmatollahi, M., Boltengagen, A., Liu, H., Hoehne, M., Rinschen, M., Schermer, B., Benzing, T., Rajewsky, N., Kocks, C., et al. (2018). A Single-Cell Transcriptome Atlas of the Mouse Glomerulus. J. Am. Soc. Nephrol. *29*, 2060–2068.

9. Qiu, C., Huang, S., Park, J., Park, Y., Ko, Y.A., Seasock, M.J., Bryer, J.S., Xu, X.X., Song, W.C., Palmer, M., et al. (2018). Renal compartment-specific genetic variation analyses identify new pathways in chronic kidney disease. Nat. Med. *24*, 1721–1731.

10. Park, J., Shrestha, R., Qiu, C., Kondo, A., Huang, S., Werth, M., Li, M., Barasch, J., and Suszták, K. (2018). Single-cell transcriptomics of the mouse kidney reveals potential cellular targets of kidney disease. Science *360*, 758–763.

11. Schell, C., Sabass, B., Helmstaedter, M., Geist, F., Abed, A., Yasuda-Yamahara, M., Sigle, A., Maier, J.I., Grahammer, F., Siegerist, F., et al. (2018). ARP3 Controls the Podocyte Architecture at the Kidney Filtration Barrier. Dev. Cell *47*, 741–757.e8.

12. Perico, L., Conti, S., Benigni, A., and Remuzzi, G. (2016). Podocyte-actin dynamics in health and disease. Nat. Rev. Nephrol. *12*, 692–710.

13. Soda, K., Balkin, D.M., Ferguson, S.M., Paradise, S., Milosevic, I., Giovedi, S., Volpicelli-Daley, L., Tian, X., Wu, Y., Ma, H., et al. (2012). Role of dynamin, synaptojanin, and endophilin in podocyte foot processes. J. Clin. Invest. *122*, 4401–4411.

14. Kliewe, F., Kaling, S., Lötzsch, H., Artelt, N., Schindler, M., Rogge, H., Schröder, S., Scharf, C., Amann, K., Daniel, C., et al. (2019). Fibronectin is up-regulated in podocytes by mechanical stress. FASEB J. *33*, 14450–14460.

15. Suleiman, H.Y., Roth, R., Jain, S., Heuser, J.E., Shaw, A.S., and Miner, J.H. (2017). Injury-induced actin cytoskeleton reorganization in podocytes revealed by super-resolution microscopy. JCI Insight *2*, 94137.

16. Rao, J., Ashraf, S., Tan, W., van der Ven, A.T., Gee, H.Y., Braun, D.A., Fehér, K., George, S.P., Esmaeilniakooshkghazi, A., Choi, W.I., et al. (2017). Advillin acts upstream of phospholipase C ε1 in steroid-resistant nephrotic syndrome. J. Clin. Invest. *127*, 4257–4269.

17. Gee, H.Y., Saisawat, P., Ashraf, S., Hurd, T.W., Vega-Warner, V., Fang, H., Beck, B.B., Gribouval, O., Zhou, W., Diaz, K.A., et al. (2013). ARHGDIA mutations cause nephrotic syndrome via defective RHO GTPase signaling. J. Clin. Invest. *123*, 3243–3253.

18. Zhu, B., Cao, A., Li, J., Young, J., Wong, J., Ashraf, S., Bierzynska, A., Menon, M.C., Hou, S., Sawyers, C., et al. (2019). Disruption of MAGI2-RapGEF2-Rap1 signaling contributes to podocyte dysfunction in congenital nephrotic syndrome caused by mutations in MAGI2. Kidney Int. *96*, 642–655.

19. Sun, H., Al-Romaih, K.I., MacRae, C.A., and Pollak, M.R. (2014). Human Kidney Disease-causing INF2 Mutations Perturb Rho/Dia Signaling in the Glomerulus. EBioMedicine *1*, 107–115.

20. Zhu, L., Jiang, R., Aoudjit, L., Jones, N., and Takano, T. (2011). Activation of RhoA in podocytes induces focal segmental glomerulosclerosis. J. Am. Soc. Nephrol. *22*, 1621–1630.

21. Blattner, S.M., Hodgin, J.B., Nishio, M., Wylie, S.A., Saha, J., Soofi, A.A., Vining, C., Randolph, A., Herbach, N., Wanke, R., et al. (2013). Divergent functions of the Rho GTPases Rac1 and Cdc42 in podocyte injury. Kidney Int. *84*, 920–930.

22. Wang, L., Ellis, M.J., Gomez, J.A., Eisner, W., Fennell, W., Howell, D.N., Ruiz, P., Fields, T.A., and Spurney, R.F. (2012). Mechanisms of the proteinuria induced by Rho GTPases. Kidney Int. *81*, 1075–1085.

23. Scott, R.P., Hawley, S.P., Ruston, J., Du, J., Brakebusch, C., Jones, N., and Pawson, T. (2012). Podocyte-specific loss of Cdc42 leads to congenital nephropathy. J. Am. Soc. Nephrol. *23*, 1149–1154.

24. Attias, O., Jiang, R., Aoudjit, L., Kawachi, H., and Takano, T. (2010). Rac1 contributes to actin organization in glomerular podocytes. Nephron, Exp. Nephrol. *114*, e93–e106.

25. Gee, H.Y., Zhang, F., Ashraf, S., Kohl, S., Sadowski, C.E., Vega-Warner, V., Zhou, W., Lovric, S., Fang, H., Nettleton, M., et al. (2015). KANK deficiency leads to podocyte dysfunction and nephrotic syndrome. J. Clin. Invest. *125*, 2375–2384.

26. Ashraf, S., Kudo, H., Rao, J., Kikuchi, A., Widmeier, E., Lawson, J.A., Tan, W., Hermle, T., Warejko, J.K., Shril, S., et al. (2018). Mutations in six nephrosis genes delineate a pathogenic pathway amenable to treatment. Nat. Commun. *9*, 1960.

27. Kaplan, J.M., Kim, S.H., North, K.N., Rennke, H., Correia, L.A., Tong, H.Q., Mathis, B.J., Rodríguez-Pérez, J.C., Allen, P.G., Beggs, A.H., and Pollak, M.R. (2000). Mutations in ACTN4, encoding alpha-actinin-4, cause familial focal segmental glomerulosclerosis. Nat. Genet. *24*, 251–256.

28. Peterson, L.C., Rao, K.V., Crosson, J.T., and White, J.G. (1985). Fechtner syndrome–a variant of Alport's syndrome with leukocyte inclusions and macrothrombocytopenia. Blood *65*, 397–406.

29. Mele, C., Iatropoulos, P., Donadelli, R., Calabria, A., Maranta, R., Cassis, P., Buelli, S., Tomasoni, S., Piras, R., Krendel, M., et al.; PodoNet Consortium (2011). MYO1E mutations and childhood familial focal segmental glomerulosclerosis. N. Engl. J. Med. *365*, 295–306.

30. Brown, E.J., Schlöndorff, J.S., Becker, D.J., Tsukaguchi, H., Tonna, S.J., Uscinski, A.L., Higgs, H.N., Henderson, J.M., and Pollak, M.R. (2010). Mutations in the formin gene INF2 cause focal segmental glomerulosclerosis. Nat. Genet. *42*, 72–76.

31. Higashi, T., Ikeda, T., Shirakawa, R., Kondo, H., Kawato, M., Horiguchi, M., Okuda, T., Okawa, K., Fukai, S., Nureki, O., et al. (2008). Biochemical characterization of the Rho GTPase-regulated actin assembly by diaphanous-related formins, mDia1 and Daam1, in platelets. J. Biol. Chem. *283*, 8746–8755.

32. Alberts, A.S. (2002). Diaphanous-related Formin homology proteins. Curr. Biol. *12*, R796.

33. Goode, B.L., and Eck, M.J. (2007). Mechanism and function of formins in the control of actin assembly. Annu. Rev. Biochem. *76*, 593–627.

34. Maiti, S., Michelot, A., Gould, C., Blanchoin, L., Sokolova, O., and Goode, B.L. (2012). Structure and activity of full-length formin mDia1. Cytoskeleton (Hoboken) *69*, 393–405.

35. Higgs, H.N. (2005). Formin proteins: a domain-based approach. Trends Biochem. Sci. *30*, 342–353.

36. Breitsprecher, D., and Goode, B.L. (2013). Formins at a glance. J. Cell Sci. *126*, 1–7.

37. Faix, J., and Grosse, R. (2006). Staying in shape with formins. Dev. Cell *10*, 693–706.

38. Chesarone, M.A., DuPage, A.G., and Goode, B.L. (2010). Unleashing formins to remodel the actin and microtubule cytoskeletons. Nat. Rev. Mol. Cell Biol. *11*, 62–74.

39. Alberts, A.S. (2001). Identification of a carboxyl-terminal diaphanous-related formin homology protein autoregulatory domain. J. Biol. Chem. *276*, 2824–2830.

40. Wallar, B.J., Stropich, B.N., Schoenherr, J.A., Holman, H.A., Kitchen, S.M., and Alberts, A.S. (2006). The basic region of the diaphanous-autoregulatory domain (DAD) is required for autoregulatory interactions with the diaphanous-related formin inhibitory domain. J. Biol. Chem. *281*, 4300–4307.

41. Li, F., and Higgs, H.N. (2003). The mouse Formin mDia1 is a potent actin nucleation factor regulated by autoinhibition. Curr. Biol. *13*, 1335–1340.

42. Moseley, J.B., Sagot, I., Manning, A.L., Xu, Y., Eck, M.J., Pellman, D., and Goode, B.L. (2004). A conserved mechanism for Bni1- and mDia1-induced actin assembly and dual regulation of Bni1 by Bud6 and profilin. Mol. Biol. Cell *15*, 896–907.

43. Pruyne, D., Evangelista, M., Yang, C., Bi, E., Zigmond, S., Bretscher, A., and Boone, C. (2002). Role of formins in actin assembly: nucleation and barbed-end association. Science *297*, 612–615.

44. Sagot, I., Rodal, A.A., Moseley, J., Goode, B.L., and Pellman, D. (2002). An actin nucleation mechanism mediated by Bni1 and profilin. Nat. Cell Biol. *4*, 626–631.

45. Sun, H., Schlondorff, J.S., Brown, E.J., Higgs, H.N., and Pollak, M.R. (2011). Rho activation of mDia formins is modulated by an interaction with inverted formin 2 (INF2). Proc. Natl. Acad. Sci. USA *108*, 2933–2938.

46. Tian, X., Kim, J.J., Monkley, S.M., Gotoh, N., Nandez, R., Soda, K., Inoue, K., Balkin, D.M., Hassan, H., Son, S.H., et al. (2014). Podocyte-associated talin1 is critical for glomerular filtration barrier maintenance. J. Clin. Invest. *124*, 1098–1113.

47. Garg, P., Verma, R., Cook, L., Soofi, A., Venkatareddy, M., George, B., Mizuno, K., Gurniak, C., Witke, W., and Holzman, L.B. (2010). Actin-depolymerizing factor cofilin-1 is necessary in maintaining mature podocyte architecture. J. Biol. Chem. *285*, 22676–22688.

48. Itoh, M., Nakadate, K., Horibata, Y., Matsusaka, T., Xu, J., Hunziker, W., and Sugimoto, H. (2014). The structural and functional organization of the podocyte filtration slits is regulated by Tjp1/ZO-1. PLoS ONE *9*, e106621.

49. Guo, B., Lyu, Q., Slivano, O.J., Dirkx, R., Christie, C.K., Czyzyk, J., Hezel, A.F., Gharavi, A.G., Small, E.M., and Miano, J.M. (2018). Serum Response Factor Is Essential for Maintenance of Podocyte Structure and Function. J. Am. Soc. Nephrol. *29*, 416–422.

50. Riedhammer, K.M., Braunisch, M.C., Günthner, R., Wagner, M., Hemmer, C., Strom, T.M., Schmaderer, C., Renders, L., Tasic, V., Gucev, Z., et al. (2020). Exome Sequencing and Identification of Phenocopies in Patients With Clinically Presumed Hereditary Nephropathies. Am. J. Kidney Dis. *76*, 460–470.

51. Zhang, L., Yang, W., Ying, D., Cherny, S.S., Hildebrandt, F., Sham, P.C., and Lau, Y.L. (2011). Homozygosity mapping on a single patient: identification of homozygous regions of recent common ancestry by using population data. Hum. Mutat. *32*, 345–353.

52. Braun, D.A., Sadowski, C.E., Kohl, S., Lovric, S., Astrinidis, S.A., Pabst, W.L., Gee, H.Y., Ashraf, S., Lawson, J.A., Shril, S., et al. (2016). Mutations in nuclear pore genes NUP93, NUP205 and XPO5 cause steroid-resistant nephrotic syndrome. Nat. Genet. *48*, 457–465.

53. Spudich, J.A., and Watt, S. (1971). The regulation of rabbit skeletal muscle contraction. I. Biochemical studies of the interaction of the tropomyosin-troponin complex with actin and the proteolytic fragments of myosin. J. Biol. Chem. *246*, 4866–4871.

54. Shekhar, S. (2017). Microfluidics-Assisted TIRF Imaging to Study Single Actin Filament Dynamics. Curr. Protoc. Cell Biol. *77*, 1–324, 24.

55. Brenner, S.L., and Korn, E.D. (1980). Spectrin/actin complex isolated from sheep erythrocytes accelerates actin polymerization by simple nucleation. Evidence for oligomeric actin in the erythrocyte cytoskeleton. J. Biol. Chem. *255*, 1670–1676.

56. Shekhar, S., and Carlier, M.F. (2017). Enhanced Depolymerization of Actin Filaments by ADF/Cofilin and Monomer Funneling by Capping Protein Cooperate to Accelerate Barbed-End Growth. Curr. Biol. *27*, 1990–1998.e5.

57. Shekhar, S., and Carlier, M.F. (2016). Single-filament kinetic studies provide novel insights into regulation of actin-based motility. Mol. Biol. Cell *27*, 1–6.

58. Schindelin, J., Arganda-Carreras, I., Frise, E., Kaynig, V., Longair, M., Pietzsch, T., Preibisch, S., Rueden, C., Saalfeld, S., Schmid, B., et al. (2012). Fiji: an open-source platform for biological-image analysis. Nat. Methods *9*, 676–682.

59. del Viso, F., and Khokha, M. (2012). Generating diploid embryos from Xenopus tropicalis. Xenopus Protocols (Totowa, NJ: Humana Press), pp. 33–41.

60. Faber, J., and Nieuwkoop, P.D. (1994). Normal Table of Xenopus Laevis (Daudin): A Systematical & Chronological Survey of the Development from the Fertilized Egg till the End of Metamorp (New York: Routledge).

61. Bhattacharya, D., Marfo, C.A., Li, D., Lane, M., and Khokha, M.K. (2015). CRISPR/Cas9: An inexpensive, efficient loss of

function tool to screen human disease genes in Xenopus. Dev. Biol. *408*, 196–204.

62. McCoy, K.E., Zhou, X., and Vize, P.D. (2011). Non-canonical wnt signals antagonize and canonical wnt signals promote cell proliferation in early kidney development. Dev. Dyn. *240*, 1558–1566.

63. Schindelin, J., Arganda-Carreras, I., Frise, E., Kaynig, V., Longair, M., Pietzsch, T., Preibisch, S., Rueden, C., Saalfeld, S., Schmid, B., et al. (2012). Fiji: an open-source platform for biological-image analysis. Nat. Methods *9*, 676–682.

64. Khokha, M.K., Chung, C., Bustamante, E.L., Gaw, L.W., Trott, K.A., Yeh, J., Lim, N., Lin, J.C., Taverner, N., Amaya, E., et al. (2002). Techniques and probes for the study of Xenopus tropicalis development. Dev. Dyn. *225*, 499–510.

65. Schirenbeck, A., Arasada, R., Bretschneider, T., Schleicher, M., and Faix, J. (2005). Formins and VASPs may co-operate in the formation of filopodia. Biochem. Soc. Trans. *33*, 1256–1259.

66. Lash, L.L., Wallar, B.J., Turner, J.D., Vroegop, S.M., Kilkuskie, R.E., Kitchen-Goosen, S.M., Xu, H.E., and Alberts, A.S. (2013). Small-molecule intramimics of formin autoinhibition: a new strategy to target the cytoskeletal remodeling machinery in cancer cells. Cancer Res. *73*, 6793–6803.

67. Vizcarra, C.L., Bor, B., and Quinlan, M.E. (2014). The role of formin tails in actin nucleation, processive elongation, and filament bundling. J. Biol. Chem. *289*, 30602–30613.

68. Gould, C.J., Maiti, S., Michelot, A., Graziano, B.R., Blanchoin, L., and Goode, B.L. (2011). The formin DAD domain plays dual roles in autoinhibition and actin nucleation. Curr. Biol. *21*, 384–390.

69. Jaiswal, R., Breitsprecher, D., Collins, A., Corrêa, I.R., Jr., Xu, M.Q., and Goode, B.L. (2013). The formin Daam1 and fascin directly collaborate to promote filopodia formation. Curr. Biol. *23*, 1373–1379.

70. Kovar, D.R., Harris, E.S., Mahaffy, R., Higgs, H.N., and Pollard, T.D. (2006). Control of the assembly of ATP- and ADP-actin by formins and profilin. Cell *124*, 423–435.

71. Jégou, A., Carlier, M.F., and Romet-Lemonne, G. (2011). Microfluidics pushes forward microscopy analysis of actin dynamics. Bioarchitecture *1*, 271–276.

72. Mu, A., Fung, T.S., Francomacaro, L.M., Huynh, T., Kotila, T., Svindrych, Z., and Higgs, H.N. (2020). Regulation of INF2-mediated actin polymerization through site-specific lysine acetylation of actin itself. Proc. Natl. Acad. Sci. USA *117*, 439–447.

73. Lee, H.K., and Deneen, B. (2012). Daam2 is required for dorsal patterning via modulation of canonical Wnt signaling in the developing spinal cord. Dev. Cell *22*, 183–196.

74. Welsh, I.C., Thomsen, M., Gludish, D.W., Alfonso-Parra, C., Bai, Y., Martin, J.F., and Kurpios, N.A. (2013). Integration of left-right Pitx2 transcription and Wnt signaling drives asymmetric gut morphogenesis via Daam2. Dev. Cell *26*, 629–644.

75. Lee, H.K., Chaboub, L.S., Zhu, W., Zollinger, D., Rasband, M.N., Fancy, S.P., and Deneen, B. (2015). Daam2-PIP5K is a regulatory pathway for Wnt signaling and therapeutic target for remyelination in the CNS. Neuron *85*, 1227–1243.

76. Ajima, R., Bisson, J.A., Helt, J.-C., Nakaya, M.-A., Habas, R., Tessarollo, L., He, X., Morrisey, E.E., Yamaguchi, T.P., and Cohen, E.D. (2015). DAAM1 and DAAM2 are co-required for myocardial maturation and sarcomere assembly. Dev. Biol. *408*, 126–139.

77. Subramanian, B., Chun, J., Perez-Gill, C., Yan, P., Stillman, I.E., Higgs, H.N., Alper, S.L., Schlöndorff, J.S., and Pollak, M.R. (2020). FSGS-Causing INF2 Mutation Impairs Cleaved INF2 N-Fragment Functions in Podocytes. J. Am. Soc. Nephrol. *31*, 374–391.

78. El-Brolosy, M.A., Kontarakis, Z., Rossi, A., Kuenne, C., Günther, S., Fukuda, N., Kikhi, K., Boezio, G.L.M., Takacs, C.M., Lai, S.L., et al. (2019). Genetic compensation triggered by mutant mRNA degradation. Nature *568*, 193–197.

79. Boyer, O., Nevo, F., Plaisier, E., Funalot, B., Gribouval, O., Benoit, G., Huynh Cong, E., Arrondel, C., Tête, M.J., Montjean, R., et al. (2011). INF2 mutations in Charcot-Marie-Tooth disease with glomerulopathy. N. Engl. J. Med. *365*, 2377–2388.